Applied Physics Letters
DOI: 10.1063/5.0078035

Platinum Nanoparticle Compression: Combining *in situ* TEM and Atomistic Modeling

Ingrid M. Padilla Espinosa[a],[1] Soodabeh Azadehranjbar[a],[2] Ruikang Ding,[2] Andrew J. Baker,[2] Tevis D.B. Jacobs*,[2] and Ashlie Martini*[1]

[1)]*Department of Mechanical Engineering, University of California, Merced, Merced, CA 95340, USA*

[2)]*Department of Mechanical Engineering and Materials Science, University of Pittsburgh, Pittsburgh, PA 15261, USA*

(*Electronic mail: amartini@ucmerced.edu)

(*Electronic mail: tjacobs@pitt.edu)

[a]I. Padilla Espinosa and S. Azadehranjbar contributed equally to this work

*Authors to whom correspondence should be addressed: Ashlie Martini, amartini@ucmerced.edu;

The mechanical behavior of nanoparticles governs their performance and stability in many applications. However, the small sizes of technologically relevant nanoparticles, with diameters in the range of 10 nm or less, significantly complicate experimental examination. These small nanoparticles are difficult to manipulate onto commercial test platforms, and deform at loads that are below the typical noise floor of the testing instruments. Here we synthesized small platinum nanoparticles directly onto a mechanical tester, and used a modified nanomanipulator to enhance load resolution to the nanonewton scale. We demonstrated the *in situ* compression of an 11.5-nm platinum nanoparticle with simultaneous high-resolution measurements of load and particle morphology. Molecular dynamics simulations were performed on similarly sized particles to achieve complementary measurements of load and morphology, along with atomic resolution of dislocations. The experimental and simulation results revealed comparable values for the critical resolved shear stress for failure, 1.28 GPa and 1.15 GPa, respectively. Overall, this investigation demonstrated the promise of, and some initial results from, the combination of atomistic simulations and *in situ* experiments with an unprecedented combination of high spatial resolution and high load resolution to understand the behavior of metal nanoparticles under compression.

Metal face-centered-cubic (FCC) nanoparticles possess unique physical, optical, electrical, and magnetic properties with applications in fields including medicine,[1] electronics,[2] water treatment,[3] and energy technologies.[4,5] Because properties depend on nanoparticle shape and size, the performance in these applications depends on the stability of the particle, and its resistance to any mechanical loading or shearing during use. Therefore, understanding the mechanical properties of metal nanoparticles is vital for controlling their performance.

Great strides have been made in the experimental measurement of the mechanical properties of metal nanoparticles, including with diamond anvil cells,[6,7] and with *in situ* compression inside a scanning electron microscope (SEM)[8,9] or a transmission electron microscope (TEM).[10–12] These techniques have been extensively applied to larger nanoparticles, with diameters in the range of tens to hundreds of nanometers, but are more challenging to apply to smaller nanoparticles with diameters in the range of 10 nm and below, so the understanding of nanoparticle deformation in this size regime remains incomplete.

TEM compression experiments, performed with real-time imaging but without any measurement of load, demonstrated that 10-nm silver nanoparticles exhibited dislocation activity during deformation that disappeared upon unloading.[13] In separate experiments, similarly sized silver nanoparticles were subjected to *in situ* TEM compression, still without load measurement, and demonstrated liquid-like behavior, where the particles recovered their original shape after the load was removed.[14] Surface diffusion was suggested as the atomic mechanism behind this liquid-like behavior. Other studies successfully employed indirect methods of *in situ* deformation of individual nanometer-sized Au and Pt crystals.[6,7,14] For example, 3.9-nm colloidal Au nanoparticles[7] were compressed under nonhydrostatic pressure conditions in an anvil cell. The structure of these particles was monitored *in situ* using a combination of x-ray diffraction and optical absorption spectroscopy, and it was shown that these particles exhibited plastic deformation due to the formation of crystalline defects (such as dislocations). However, it was not possible to observe the defects in real time. These investigations open up intriguing questions about the deformation mechanisms of these particles, yet the former experiments lacked accurate load measurements, while the latter experiments lacked *in situ* visualization of the particles.

Compression of small metal FCC nanoparticles has also been studied with simulation methods such as density functional theory (DFT), molecular dynamics (MD), and finite element methods (FEM).[15,16] Among these methods, DFT calculations are usually limited to small numbers of atoms because of the high computational cost, and FEM simulations include continuum assump-

tions that may not be valid at the nanoscale, and also cannot provide atomic resolution.[15] MD allows the modeling of nanoparticles of different sizes and geometries at the atomic level, with a reasonable computational cost.[17] Previous MD models of metal FCC nanoparticles found that nanoparticles exhibit elasticity at low stress[18–20]. Then, higher stress was shown to cause the nucleation of Shockley $1/6\langle 112\rangle\{111\}$ partial dislocations, phase changes, and atom rearrangement, especially at the corners and edges of faceted metal FCC nanoparticles.[20–22]

Several studies[7,9,10,21] have combined experimental (diamond anvil cell, *in situ* TEM/SEM indentation) compression of metal FCC nanoparticles with MD simulations. The computational models were used to simulate dislocations and stacking faults caused by compression. Two types of stacking faults arose from the nucleation and propagation of Shockley partial dislocations: parallel to the surface of the nanostructure or parallel to internal twin boundaries. In these studies, the computational models provided the atomic resolution that could not be fully observed experimentally. However, the investigations suffered the same limitations discussed earlier: the diamond-anvil-cell method lacked direct visualization of nanoparticles, while the *in situ* TEM investigations only provided direct force measurement for large nanoparticles. The challenges in conducting experimental (or combined experimental and simulation) investigations on small nanoparticles stem from typical *in situ* apparatus and methodology. The most commonly used approach is to synthesize particles and drop-cast them onto the gauge section of a commercial *in situ* TEM nanoindenter. However, as particles shrink down to 10 nm and below, a scale that is critically important for practical applications,[1,23–26] this approach becomes increasingly difficult to perform for two reasons: First, it is difficult to deposit small particles in the ideal test configuration, i.e., isolated particles located in a region that is visible and accessible by the indenter. Second, the loads at which very small particles deform (often in the tens of nanonewtons) are smaller than the noise floors of commercial *in situ* TEM nanoindenters (typically in the hundreds or even thousands of nanonewtons). Here, we overcome these limitations and demonstrate the simultaneous visualization and load measurement for deformation of an 11.5-nm-diameter platinum nanoparticle. Then we use complementary atomistic simulations to understand the deformation behavior.

To overcome the difficulty of placing nanoparticles in a specific location for testing, we synthesized the platinum particles directly on the testing substrate using strong electrostatic absorption (SEA).[27] SEA is a wet-chemistry method that utilizes electrostatic absorption between the surface of a substrate and charged metal complex in solution to deposit nanoparticles. Six steps were involved, similar to the standard protocol of Ref[27], and so they are only briefly described

here. First, a plasma-cleaned silicon thin-wedge TEM substrate (<200 nm Plateau, Bruker, Bullerica, MA), with plateau thickness of approximately 10 nm, was oxidized to form a silica wedge by annealing in air atmosphere at 800 ºC with a flow rate of 0.05 cm^2/min and heating rate of 10 ºC/min for 30 minutes. Second, metal precursors (tetraammineplatinum(II) hydroxide hydrate ($Pt(NH_3)_4(OH)_2 \cdot xH_2O$) from Sigma-Aldrich) were added to the deionized water with an approximate concentration of 2.5 mg per 10 mL of deionized water. The low concentration resulted in a homogeneous distribution of nanoparticles. Third, the pH was adjusted to 12 by addition of NaOH. Fourth, the oxidized wedges were impregnated with the solution for 1 hr. Then, the wedges were calcinated at high temperature (675 ºC) in a tube furnace (Lindberg/Blue M, Thermo Electron, Waltham, MA) for three hours with a heating rate of 10 ºC/min and flow rate of 0.05 cm^3/min to disrupt the strong metal complex-substrate interactions that control nanoparticle size.[28] Lastly, the impregnated wedges were hydrogenated at moderate temperature (250 ºC) in 10% H_2/Ar atmosphere for two hours with a heating rate of 5 ºC/min and flow rate of 0.5 cm^3/min to reduce the nanoparticles and remove any surface oxide from the oxidation step. In general, this technique produces bare nanoparticles that are free of the surface ligands that are typical for commercially available particles.

Small platinum nanoparticles were compressed using a modified commercial *in situ* TEM nanomanipulator (Biasing Manipulator model 1800, Hummingbird Scientific, Lacey, WA) in a transmission electron microscope (Titan Themis G2 200, ThermoFisher Scientific, Waltham, MA) at an accelerating voltage of 200 kV. While this nanomanipulator cannot inherently measure loads, it provides the precision of movement required for small-nanoparticle compression. The load measurement challenge was overcome by modifying the manipulator to include an atomic force microscope probe, which served as indenter and load sensor.[29–31] The cantilever stiffness of the probe was pre-calibrated using the Sader method[32] and the spring constant was found to be 37.4 N/m. The nanoparticle-coated substrate was mounted on the piezo-controlled arm, and advanced towards the nanoscale tip of the atomic force microscope probe at a rate of 0.5 nm/s to load the nanoparticle up to a force of 169 ± 3 nN and then retracted to separation. In order to minimize the effect of the electron beam on the nanoparticles, the beam intensity used in our experiments was kept less than 7000 $e/s\text{Å}^2$ (11 A/cm^2) which is considered "very weak beam" (beam intensities < 10000 $e/s\text{Å}^2$) according to prior literature. [33] Additionally, direct visual observation of particle behavior before and after to loading indicated an absence of beam damage or modification for these and other tested particles.

During the tests, real-time TEM videos were recorded. Calculation of load and deformation was performed after the test using image analysis and digital image correlation (DIC) methods. Because of the sub-pixel resolution of DIC measurement,[34] this technique is able to track the motion of the indenter with an accuracy of approximately 0.025 nm. When combined with the spring constant of the cantilever, this achieves a load resolution of 1 nN. Therefore, the approach is capable of combining nanonewton load resolution with the Ångström-scale spatial resolution that is required to reveal the behavior of ultra-small nanoparticles.

The loading data obtained from *in situ* TEM compression of a Pt nanoparticle of diameter 11.5 nm is shown in Fig. 1(a), with nanoparticle morphologies at representative times shown in Figs. 1(b)-(d) (Video S1 in supplementary materials Multimedia View). When the probe reached a distance of 0.5 nm from the nanoparticle, van der Waals attraction resulted in a snap-in event with an adhesive force of -15.3 ± 0.1 nN (Fig. 1(b)). No deformation was visible during the snap-in event.

After contact, the force was gradually increased up to a maximum of 169 ± 3 nN. Some surface rearrangement was observed from the jagged sides of nanoparticle (see the yellow arrows in Fig. 1(c)). The precise cause of this rearrangement cannot be determined from the present test and may indicate some local rearrangement of preexisting dislocations or twin boundaries prior to the initiation of the system-spanning slip event that caused catastrophic failure. The force then dropped suddenly and the Pt nanoparticle failed through a catastrophic slip event that spanned the entire particle (dashed yellow line in Fig. 1(d)). Based on the observation of failure and orientation of the nanoparticle, determined from the fast Fourier transformation (FFT) pattern of the nanoparticle before failure (See Figure S2), the slip plane was determined to be of {1 1 1} type. This slip event led to a sharp force drop to 37 ± 4 nN as seen in Fig. 1(a).

The critical resolved shear stress (CRSS) at which the nanoparticle failed was calculated using Schmid's law[35]:

$$CRSS = \frac{F}{A}\cos\phi\cos\lambda \tag{1}$$

where F is the measured force at failure, A is the cross-sectional area, ϕ is the angle between the force direction and the vector normal to the shear plane, and λ is the angle between the force and the shear direction, see Fig. 1(d).

To calculate area $\boldsymbol{A}$ in Eq. 1, the width of the nanoparticle was measured, and a circular cross-section was assumed. Because the width varies across the nanoparticle, different values of $\boldsymbol{A}$ can be obtained; however, using the observed location where the slip plane intersects the surface

(and also assuming that the dislocation nucleates where the resolved shear stress is highest) the cross-sectional area was calculated based on the location of catastrophic failure, corresponding to the left side of the nanoparticle near the bottom surface (bottommost arrow in Fig. 1c). Using this approach, the nanoparticle failure occurred at a CRSS of 1.28 GPa.

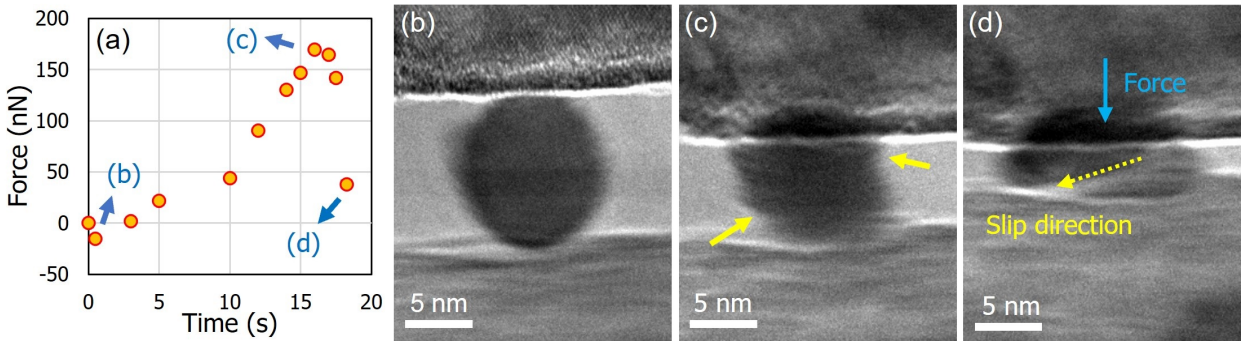

FIG. 1. An 11.5-nm nanoparticle was compressed to failure with simultaneous high-resolution measurements of load (a) and morphology (b-d). The particle showed no visible deformation upon the initial contact (a), with some surface rearrangement occurring during loading (c). Catastrophic failure occurred (d) via deformation along a particle-spanning slip plane.

MD simulations were performed using the Large-scale Atomic/Molecular Massively Parallel Simulator (LAMMPS) package.[36] Based on the apparent shape from the *in situ* TEM, a near-spherical model FCC nanoparticle with an equivalent diameter of 11.5 nm was "carved" from a platinum crystal with faces oriented in the {111} plane, using the LAMMPS package and the visualization software Ovito.[37]. The atomic interactions were described by the embedded atom method (EAM),[38] using a parameterization which was shown to accurately reproduce the mechanical and surface properties of bulk and nanoscale platinum.[39] A 10-nm gap was introduced between the nanoparticle and the edges of the simulation box to allow for atom mobility and deformation in response to compression, and fixed boundary conditions were applied in all directions. The nanoparticle was initially geometrically optimized using the conjugate gradient method until the difference in energy between iterations divided by average energy was less than $1x10^{-7}$. The temperature of the system was increased to 298 K and equilibrated for 200 ps using a canonical ensemble with a Langevin thermostat.

To apply compression, two movable virtual flat walls were placed at the top and bottom of the simulation box. These walls interacted with the nanoparticle atoms following a Lennard–Jones 9-3 potential[40] with epsilon equal to 0.6 eV, sigma equal to 0.06 nm, and a cutoff of 0.25 nm.

Different Lennard-Jones parameters were tested and no effect on the nanoparticle force response was observed. To reduce the effect of strain rate, the compression was imposed in a step-wise manner: First, the walls moved in opposite directions towards the nanoparticle at a constant rate of 0.2×10^{-4} nm.ps^{-1} in steps of 40 ps. Then, each compression step was followed by an equilibration period of 50 ps using a canonical ensemble, allowing atomic relaxation between compression steps. The force was calculated as the reaction force exerted on the virtual walls averaged over the last 12 ps at each equilibration period following the compression. A timestep of 1 fs was used for all the dynamics processes.

The loading data obtained from the MD simulation of the compression of the 11.5 nm nanoparticle is shown in Fig. 2(a). While the experimental force curve in Fig. 1(a) shows a catastrophic failure at the maximum load, the simulated force curve in Fig. 2(a) shows a long period of continuous deformation. These different behaviors reflect the different methods of control. The simulation was run in displacement control, where dislocation activity could cause load drops. However, in the *in situ* TEM compression, the cantilever-based spring constant was maintaining an approximately constant load at the point of dislocation nucleation. In this case, all subsequent lower-stress deformation took place suddenly, and the particle was immediately crushed. While these force curves are scientifically compatible, the simulated force curve enabled far richer analysis of the behavior during compression.

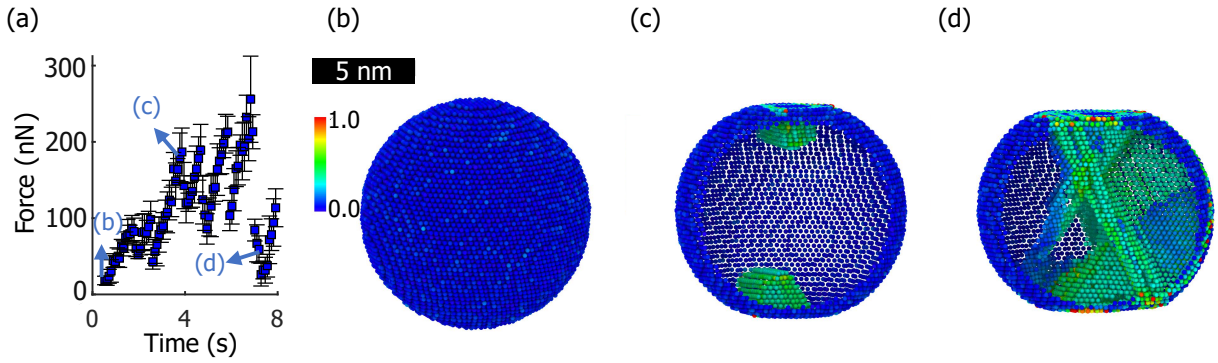

FIG. 2. The force (a) on a model nanoparticle (b) of similar shape and size as the experiment during a compression simulation. The instantaneous particle morphology is shown using a slice through the particle perpendicular to the (010) plane at initial contact (c), during loading (d), and after failure, where failure is identified as a significant load drop almost to zero. Atoms in (b-d) are colored by atomic strain, with atoms having a strain lower than 0.3 hidden to facilitate the visualization

The MD force-vs.-time curve (Fig. 2(a)) showed various load-drop events, with some at lower force ($\approx$ 100 nN) and others at higher force ($\approx$ 200 nN). The cross-sections of the particle indicated that the lower-force load-drop events were associated with surface rearrangement near the indenter walls, and did not represent deformation in the bulk of the particle. By contrast, at the higher-force load-drop events, the atomic shear strain indicated that dislocation activity was initiated at the regions of high atomic strain near the surface, and these dislocations propagated as a pyramidal structure towards the center of the nanoparticle. This strain was accompanied by the nucleation of Shockley dislocations. As the dislocations nucleated and propagated, the strain increased and planes of deformation were observed (Fig. 2(d)).

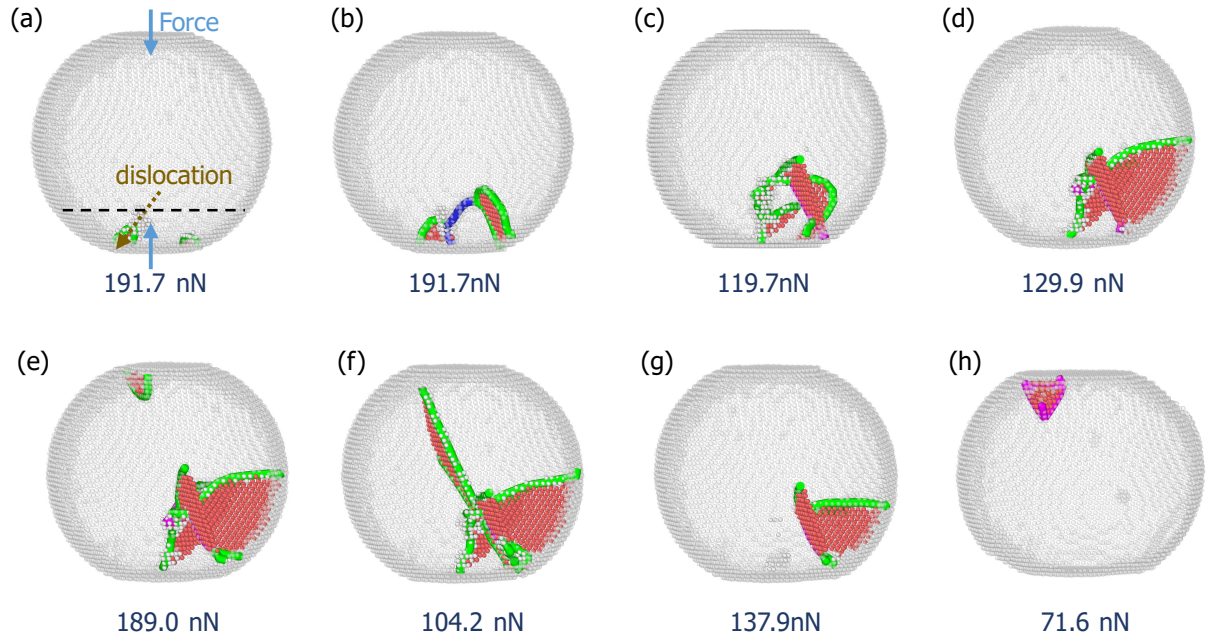

FIG. 3. Snapshots of the dislocation nucleation and dislocation glide. Perfect FCC crystal atoms are hidden to facilitate visualization. Red spheres correspond to hexagonal close-packed (HCP) atoms, and white spheres are atoms with amorphous structure. Shockley dislocation are shown as green tubes, Stair-rod as magenta tubes, and Perfect as blue tubes.

The MD simulations provide detailed atomic information about the nucleation and propagation of dislocations, as well as the failure mechanisms of the nanoparticle. A detailed dislocation analysis illustrating the structure and dislocations of the nanoparticle at different compression stages is shown in Fig. 3.

At the maximum force of the pre-dislocation region (191.7 nN), two Shockley dislocations,

shown in green in Fig. 3(a), nucleated from the surface of the nanoparticle. These dislocations propagated through the nanoparticle towards an opposite surface, and a perfect dislocation appeared without further increment of the enforced displacement (Fig. 3(b)). As the dislocations propagated, the force dropped, and a larger number of atoms transitioned to an HCP configuration, or to amorphous arrangements (Fig. 3(c)). Next, the force increased as the atoms accommodated the strain and the dislocations glided from the nucleation site to escape towards the surfaces (Fig. 3(d)). Once a maximum force was achieved, new Shockley dislocations nucleated from the top surface at the second force peak at 189.0 nN (Fig. 3(e)). These newly formed dislocations glided towards the lower surface (Fig. 3(f)). Some dislocations escaped from the surface and the load increased as shown in Figure (Fig. 3(g)). The processes of dislocation nucleation and gliding towards the nanoparticle surface continued as the compression progressed, leaving behind surface steps as shown in (Fig. 3(h)).

To compute the CRSS, Schmid's law Eq. 1 was used to analyze the computational models exactly as it was done for experiments. The stress was calculated using the maximum force before significant dislocation-mediated load drops occurred and the cross-sectional area at which the initial dislocations nucleated, shown with a black dotted line in Fig. 3(a). While the TEM only provided a 2D view, the MD provided a full 3D analysis at the atomic level, and the dislocation evolution below the nanoparticle surface could also be observed. Indeed, multiple Shockley dislocations were observed nucleating and propagating during the transition from homogeneous to dislocation-mediated deformation. To determine the CRSS, we calculated the angle of the Burgers vectors with respect to the force for the initial two dislocations shown in Fig. 3(a). Slip along the {1 1 1} or {1 0 0} planes is expected with close-packed planes in FCC metals.[41] In this case, the slip planes were identified based on the deformed structure where a dislocation occurred and corresponded to {1 1 1} planes, (See Figure S3). Based on the determined Burgers vector $1/6[-1-12]$, and slip plane (1 1 1), a CRSS value of 1.15 GPa was calculated. This value is in a similar range to that calculated from the experimental data (1.28 GPa), suggesting that the approach used to estimate the CRSS from MD simulations can be applied for this analysis.

Although values of the CRSS for platinum nanoparticles in the range of 10 nm have not been reported previously, the values obtained here are within the range reported in previous studies on FCC micro- and nanostructures as shown in table S1 in supplementary material. These earlier investigations include experimental studies on platinum nanoparticles in the size range of 150 - 620 nm (maximum CRSS 2.1 GPa)[8], nickel nanoparticles in the size range of 200 - 1000 nm

(CRSS between 2.5 and 10 GPa),[9] molybdenum nanopillars of 100 nm diameter (CRSS 1 GPa)[42] and copper, aluminum, and iron nanopillars (CRSS above 0.5 GPa) for diameters less than 100 nm by curve extrapolation,[43] and FEM simulations on gold microparticles with maximum diameter of 1 micron (CRSS 1.3 ± 0.2 GPa).[21]

Previous studies on the compression strength of metal nanoparticles demonstrated that nanoparticle strength increases with decreasing size following a power law.[8,21,44,45] However, it has been observed that there is a critical size below which a strength saturation is reached.[8,44] Our calculated CRSS is comparable to the CRSS of larger platinum nanoparticles reported previously (maximum CRSS 2.1 GPa for nanoparticles diameters between 150-620 nm).[8] This suggests that saturation of the compressive strength was reached with the 10 nm particle studied here, and that the strength would not increase for smaller sizes. Future studies may explore the effect of length scale by analyzing the CRSS from compression of nanoparticles of different sizes.

In conclusion, combined *in situ* TEM experiments and MD simulations demonstrated the behavior of small platinum nanoparticles under compression with simultaneous measurement of nanonewton-scale loads and Ångström-scale changes in particle size, shape, and defect evolution. Both experiments and simulations gave approximately the same CRSS value, which confirmed the applicability of the simulations such that they could be used to reveal atomistic mechanisms of deformation and failure. More generally, this study showed the range of deformation mechanisms and nanoscale effects that govern the behavior of technologically relevant nanoparticles.

SUPPLEMENTARY MATERIAL

See the supplementary material for: a video of the *in situ* TEM compression of the platinum nanoparticle "Multimedia view". Figure S2: Fast Fourier transformation of the compressed nanoparticle showing the lattice fringes used to determine the nanoparticle orientation. Figure S3: Illustration of the {111} planes used to calculate the CRSS from molecular dynamics simulations. Table S1: Critical resolved shear stress for representative metal nanomaterials and bulk FCC metals.

ACKNOWLEDGMENTS

We wish to acknowledge the support of the U.S. Department of Energy, Office of Science, Office of Basic Energy Sciences, under Award No. DE-SC0021155. This research also used resources of the National Energy Research Scientific Computing Center, a DOE Office of Science User Facility supported by the Office of Science of the U.S. Department of Energy under Contract No. DE-AC02-05CH11231. The authors would like to thank Götz Vezer and Sanjana Karpe at the University of Pittsburgh for assistance with nanoparticle synthesis. The authors acknowledge the use of the Nanoscale Fabrication and Characterization Facility (NFCF) in the Gertrude E. & John M. Petersen Institute of Nanoscience and Engineering and Materials Micro-characterization Lab (MMCL) in Swanson School of Engineering.

DATA AVAILABILITY STATEMENT

The data that support the findings of this study are available from the corresponding author upon reasonable request.

REFERENCES

[1]M. Rai, A. P. Ingle, S. Birla, A. Yadav, and C. A. D. Santos, "Strategic role of selected noble metal nanoparticles in medicine," Crit. Rev. Microbiol. **42**, 696–719 (2016).

[2]M. Zebarjadi, K. Esfarjani, A. Shakouri, J.-H. Bahk, Z. Bian, G. Zeng, J. Bowers, H. Lu, J. Zide, and A. Gossard, "Effect of nanoparticle scattering on thermoelectric power factor," Appl. Phys. Lett. **94**, 202105 (2009).

[3]R. R. Gadkari, S. W. Ali, R. Alagirusamy, and A. Das, "Silver nanoparticles in water purification: Opportunities and challenges," in *Modern Age Environmental Problems and their Remediation*, edited by M. Oves, M. Zain Khan, and I. M.I. Ismail (Springer International Publishing, 2018) pp. 229–237.

[4]Y. G. Liu, S. L. Shi, X. Y. Xue, J. Y. Zhang, Y. G. Wang, and T. H. Wang, "Edge–truncated cubic platinum nanoparticles as anode catalysts for direct methanol fuel cells," Appl. Phys. Lett. **92**, 203105 (2008).

[5]Y. Chen, Y. Zhai, L. Deng, N. Wang, Y. Mao, J. Yang, and Y. Huang, "Optimizing ag–pt core–shell nanostructures for solar energy conversion, plasmonic photocatalysis, and photothermal catalysis," Appl. Phys. Lett. **114**, 183902 (2019).

[6]X. W. Gu, L. A. Hanson, C. N. Eisler, M. A. Koc, and A. P. Alivisatos, "Pseudoelasticity at large strains in au nanocrystals," Phys. Rev. Lett. **121**, 056102 (2018).

[7]A. Parakh, S. Lee, K. A. Harkins, M. T. Kiani, D. Doan, M. Kunz, A. Doran, L. A. Hanson, S. Ryu, and X. W. Gu, "Nucleation of Dislocations in 3.9 nm Nanocrystals at High Pressure," Phys. Rev. Lett **124**, 106104 (2020).

[8]J. Zimmerman, A. Bisht, Y. Mishin, and E. Rabkin, "Size and shape effects on the strength of platinum nanoparticles," J. Mater. Sci (2021), 10.1007/s10853-021-06435-7.

[9]A. Sharma, J. Hickman, N. Gazit, E. Rabkin, and Y. Mishin, "Nickel nanoparticles set a new record of strength," Nat. Commun. **9**, 4102 (2018).

[10]G. Casillas, J. P. Palomares-Báez, J. L. Rodríguez-López, J. Luo, A. Ponce, R. Esparza, J. J. Velázquez-Salazar, A. Hurtado-Macias, J. González-Hernández, and M. José-Yacaman, "In situ tem study of mechanical behaviour of twinned nanoparticles," Philos. Mag **92**, 4437–4453 (2012).

[11]D. Mordehai, O. David, and R. Kositski, "Nucleation–controlled plasticity of metallic nanowires and nanoparticles," Adv. Mater **30**, 1706710 (2018).

[12]A. Nafari, D. Karlen, C. Rusu, K. Svensson, H. Olin, and P. Enoksson, "Mems sensor for *In Situ* tem atomic force microscopy," J. Microelectromech. Syst. **17**, 328–333 (2008).

[13]C. Carlton and P. Ferreira, "In situ tem nanoindentation of nanoparticles," Micron **43**, 1134–1139 (2012), in situ TEM.

[14]J. Sun, L. He, Y.-C. Lo, T. Xu, H. Bi, L. Sun, Z. Zhang, S. X. Mao, and J. Li, "Liquid–like pseudoelasticity of sub–10–nm crystalline silver particles," Nat. Mater **13**, 1007–1012 (2014).

[15]J. Amodeo and L. Pizzagalli, "Modeling the mechanical properties of nanoparticles: a review," Comptes Rendus. Physique (2021), 10.5802/crphys.70, online first.

[16]P. Armstrong and W. Peukert, "Size effects in the elastic deformation behavior of metallic nanoparticles," J. Nanopart. Res. **14**, 1288 (2012).

[17]P. Tian, "Molecular dynamics simulations of nanoparticles," Annu. Rep. Prog. Chem., Sect. C: Phys. Chem. **104**, 142–164 (2008).

[18]L. Yang, J.-J. Bian, and G.-F. Wang, "Impact of atomic–scale surface morphology on the size-dependent yield stress of gold nanoparticles," J. Phys. D: Appl. Phys **50**, 245302 (2017).

[19]L. Yang, J. Feng, Y. Ding, J. J. Bian, and G. F. Wang, "An analytical description for the elastic compression of metallic polyhedral nanoparticles," AIP Adv. **6**, 085113 (2016).

[20]Y. Feruz and D. Mordehai, "Towards a universal size–dependent strength of face-centered cubic nanoparticles," Acta Mater. **103**, 433–441 (2016).

[21]D. Mordehai, S.-W. Lee, B. Backes, D. J. Srolovitz, W. D. Nix, and E. Rabkin, "Size effect in compression of single-crystal gold microparticles," Acta Mater. **59**, 5202–5215 (2011).

[22]J. Amodeo and K. Lizoul, "Mechanical properties and dislocation nucleation in nanocrystals with blunt edges," Mater. & Des. **135**, 223–231 (2017).

[23]R. M. Rioux, H. Song, P. Yang, and G. A. Somorjai, "Chapter 7 - platinum nanoclusters' size and surface structure sensitivity of catalytic reactions," in *Met. Nanoclusters Catal. Mater. Sci.: Issue Size Control*, edited by B. Corain, G. Schmid, and N. Toshima (Elsevier, Amsterdam, 2008) pp. 149–166.

[24]X. Jiang, B. Du, Y. Huang, and J. Zheng, "Ultrasmall noble metal nanoparticles: Breakthroughs and biomedical implications," Nano Today **21**, 106–125 (2018).

[25]X. Huang, C. Guo, J. Zuo, N. Zheng, and G. D. Stucky, "An assembly route to inorganic catalytic nanoreactors containing sub-10-nm gold nanoparticles with anti-aggregation properties," Small **5**, 361–365 (2009).

[26]S. Hwang, J. Nam, J. Song, S. Jung, J. Hur, K. Im, N. Park, and S. Kim, "A sub 6 nanometer plasmonic gold nanoparticle for ph-responsive near-infrared photothermal cancer therapy," New J. Chem. **38**, 918–922 (2014).

[27]L. Jiao and J. R. Regalbuto, "The synthesis of highly dispersed noble and base metals on silica via strong electrostatic adsorption: I. amorphous silica," J. Catal **260**, 329–341 (2008).

[28]J. T. Miller, M. Schreier, A. J. Kropf, and J. R. Regalbuto, "A fundamental study of platinum tetraammine impregnation of silica: 2. The effect of method of preparation, loading, and calcination temperature on (reduced) particle size," J. Catalysis **225**, 203–212 (2004).

[29]S. B. Vishnubhotla, S. R. Khanal, J. Li, E. A. Stach, and T. D. B. Jacobs, "Investigating load-dependent conduction through platinum nanocontacts using in situ electromechanical testing inside a transmission electron microscope," in *2017 IEEE 17th International Conference on Nanotechnology (IEEE-NANO)* (2017) pp. 130–134.

[30]S. B. Vishnubhotla, C. R., S. R. Khanal, J. Li, E. A. Stach, A. Martini, and T. D. B. Jacobs, "Quantitative measurement of contact area and electron transport across platinum nanocontacts for scanning probe microscopy and electrical nanodevices," Nanotechnology **30**, 045705 (2018).

[31]S. B. Vishnubhotla, C. R., S. R. Khanal, X. Hu, A. Martini, and T. D. B. Jacobs, "Matching Atomistic Simulations and In Situ Experiments to Investigate the Mechanics of Nanoscale Contact," Tribol. Lett. **67**, 97 (2019).

[32]J. E. Sader, J. W. Chon, and P. Mulvaney, "Calibration of rectangular atomic force microscope cantilevers," Rev. Sci. Instrum. **70**, 3967–3969 (1999).

[33]J.-O. Bovin and J.-O. Malm, "Atomic resolution electron microscopy of small metal clusters," Zeitschrift für Physik D Atoms, Molecules and Clusters **19**, 293–298 (1991).

[34]P. Bing, X. Hui-min, X. Bo-qin, and D. Fu-long, "Performance of sub-pixel registration algorithms in digital image correlation," Meas. Sci. Technol **17**, 1615–1621 (2006).

[35]E. Schmid and W. Boas, *Plasticity of Crystals with Special Reference to Metals* (F.A. Hughes, 1950).

[36]S. Plimpton, "Fast Parallel Algorithms for Short-Range Molecular Dynamics," J. Comput. Phys. **117**, 1–19 (1995).

[37]A. Stukowski, "Visualization and analysis of atomistic simulation data with OVITO-the Open Visualization Tool," Model. Simul. Mater. Sci. Eng **18** (2010), 10.1088/0965-0393/18/1/015012.

[38]X. W. Zhou, R. A. Johnson, and H. N. G. Wadley, "Misfit-energy-increasing dislocations in vapor-deposited CoFe/NiFe multilayers," Phys. Rev. B **69**, 144113 (2004).

[39]I. M. Padilla Espinosa, T. D. B. Jacobs, and A. Martini, "Evaluation of Force Fields for Molecular Dynamics Simulations of Platinum in Bulk and Nanoparticle Forms," J. Chem. Theory Comput. (2021), 10.1021/acs.jctc.1c00434.

[40]H. Heinz, R. A. Vaia, B. L. Farmer, and R. R. Naik, "Accurate Simulation of Surfaces and Interfaces of Face-Centered Cubic Metals Using 12-6 and 9-6 Lennard-Jones Potentials," J. Phys. Chem. C **112**, 17281–17290 (2008).

[41]A. G. Jackson, "Slip Systems BT - Handbook of Crystallography: For Electron Microscopists and Others," (Springer New York, New York, NY, 1991) pp. 83–88.

[42]A. Schneider, B. Clark, C. Frick, P. Gruber, and E. Arzt, "Effect of orientation and loading rate on compression behavior of small-scale mo pillars," Mater. Sci. Eng. A . **508**, 241–246 (2009).

[43]M. Mlikota and S. Schmauder, "On the critical resolved shear stress and its importance in the fatigue performance of steels and other metals with different crystallographic structures," Metals **8**, 883 (2018).

[44]T. J. Flanagan, O. Kovalenko, E. Rabkin, and S.-W. Lee, "The effect of defects on strength of gold microparticles," Scr. Mater. **171**, 83–86 (2019).

[45]J. R. Greer, W. C. Oliver, and W. D. Nix, "Size dependence of mechanical properties of gold at the micron scale in the absence of strain gradients," Acta Mater. **53**, 1821–1830 (2005).

[46]Z. W. Shan, G. Adesso, A. Cabot, M. P. Sherburne, S. A. Syed Asif, O. L. Warren, D. C. Chrzan, A. M. Minor, and A. P. Alivisatos, "Ultrahigh stress and strain in hierarchically structured hollow nanoparticles," Nat. Mater **7**, 947–952 (2008).

[47]E. Calvié, J. Réthoré, L. Joly-Pottuz, S. Meille, J. Chevalier, V. Garnier, Y. Jorand, C. Esnouf, T. Epicier, J. Quirk, and K. Masenelli-Varlot, "Mechanical behavior law of ceramic nanoparticles from transmission electron microscopy in situ nano–compression tests," Mater. Lett. **119**, 107–110 (2014).

[48]L. Sun, A. V. Krasheninnikov, T. Ahlgren, K. Nordlund, and F. Banhart, "Plastic deformation of single nanometer-sized crystals," Phys. Rev. Lett. **101**, 156101 (2008).

[49]G. Guisbiers, S. Mejía-Rosales, and F. Leonard Deepak, "Nanomaterial Properties: Size and Shape Dependencies," J. Nanomater. **2012**, 180976 (2012).

[50]J. E. De Vrieze, G. M. Bremmer, M. Aly, V. Navarro, J. W. Thybaut, P. J. Kooyman, and M. Saeys, "Shape of Cobalt and Platinum Nanoparticles Under a CO Atmosphere: A Combined In Situ TEM and Computational Catalysis Study," ACS Catalysis **9**, 7449–7456 (2019).

[51]M. Ahmadi, J. Timoshenko, F. Behafarid, and B. Roldan Cuenya, "Tuning the Structure of Pt Nanoparticles through Support Interactions: An in Situ Polarized X-ray Absorption Study Coupled with Atomistic Simulations," J. Phys. Chem. C **123**, 10666–10676 (2019).

[52]J. Wu, W. Gao, H. Yang, and J.-M. Zuo, "Dissolution Kinetics of Oxidative Etching of Cubic and Icosahedral Platinum Nanoparticles Revealed by in Situ Liquid Transmission Electron Microscopy," ACS Nano **11**, 1696–1703 (2017).

[53]H. Song, F. Kim, S. Connor, G. A. Somorjai, and P. Yang, "Pt Nanocrystals: Shape Control and Langmuir–Blodgett Monolayer Formation," J. Phys. Chem. B **109**, 188–193 (2004).

[54]R. Narayanan and M. A. El-Sayed, "Shape-Dependent Catalytic Activity of Platinum Nanoparticles in Colloidal Solution," Nano Letters **4**, 1343–1348 (2004).

[55]S. D. Perrault and W. C. W. Chan, "Synthesis and Surface Modification of Highly Monodispersed, Spherical Gold Nanoparticles of 50–200 nm," J. Am. Chem. Soc. **131**, 17042–17043 (2009).

[56]G. Wang, J. Bian, J. Feng, and X. Feng, "Compressive behavior of crystalline nanoparticles with atomic-scale surface steps," Mater. Res. Express **2**, 015006 (2014).

[57]Z. Li, Y. Gao, S. Zhan, H. Fang, and Z. Zhang, "Molecular dynamics study on temperature and strain rate dependences of mechanical properties of single crystal al under uniaxial loading," AIP Adv. **10**, 075321 (2020).

[58]S. J. A. Koh and H. P. Lee, "Molecular dynamics simulation of size and strain rate dependent mechanical response of fcc metallic nanowires," Nanotechnology **17**, 3451–3467 (2006).

[59]W. Wang, M. Wang, E. Ambrosi, A. Bricalli, M. Laudato, Z. Sun, X. Chen, and D. Ielmini, "Surface diffusion-limited lifetime of silver and copper nanofilaments in resistive switching devices," Nat. Commun. **10**, 81 (2019).

[60]N. Combe, P. Jensen, and A. Pimpinelli, "Changing shapes in the nanoworld," Phys. Rev. Lett. **85**, 110–113 (2000).

[61]D. Holec, P. Dumitraschkewitz, D. Vollath, and F. D. Fischer, "Surface energy of au nanoparticles depending on their size and shape," Nanomaterials **10** (2020).

[62]J. Gezelter, S. Kuang, J. Marr, K. Stocker, C. Li, C. Vardeman, T. Lin, C. Fennell, X. Sun, K. Daily, *et al.*, "Openmd, an open source engine for molecular dynamics," University of Notre Dame, Notre Dame, IN (2010).

[63]C. H. B. Ng, J. Yang, and W. Y. Fan, "Synthesis and self-assembly of one-dimensional sub-10 nm ag nanoparticles with cyclodextrin," J. Phys. Chem. C **112**, 4141–4145 (2008).

[64]M. P. Melancon, W. Lu, and C. Li, "Gold-based magneto/optical nanostructures: challenges for in vivo applications in cancer diagnostics and therapy," MRS Bull. **34**, 415–421 (2009).

[65]A. Kunz, S. Pathak, and J. R. Greer, "Size effects in al nanopillars: Single crystalline vs. bicrystalline," Acta Mater. **59**, 4416–4424 (2011).